Defect-mediated transport and electronic irradiation effect in individual domains of CVD-grown monolayer MoS_2

Corentin Durand, Xiaoguang Zhang, and Jason Fowlkes
Center for Nanophase Materials Sciences, Oak Ridge National Laboratory, Oak Ridge, Tennessee 37831

Sina Najmaei and Jun Lou
Department of Materials Science and NanoEngineering, Rice University, Houston, Texas 77251

An-Ping Li[a)]
Center for Nanophase Materials Sciences, Oak Ridge National Laboratory, Oak Ridge, Tennessee 37831

(Received 10 October 2014; accepted 7 January 2015; published 16 January 2015)

The authors study the electrical transport properties of atomically thin individual crystalline grains of MoS_2 with four-probe scanning tunneling microscopy. The monolayer MoS_2 domains are synthesized by chemical vapor deposition on SiO_2/Si substrate. Temperature dependent measurements on conductance and mobility show that transport is dominated by an electron charge trapping and thermal release process with very low carrier density and mobility. The effects of electronic irradiation are examined by exposing the film to electron beam in the scanning electron microscope in an ultrahigh vacuum environment. The irradiation process is found to significantly affect the mobility and the carrier density of the material, with the conductance showing a peculiar time-dependent relaxation behavior. It is suggested that the presence of defects in active MoS_2 layer and dielectric layer create charge trapping sites, and a multiple trapping and thermal release process dictates the transport and mobility characteristics. The electron beam irradiation promotes the formation of defects and impact the electrical properties of MoS_2. Our study reveals the important roles of defects and the electron beam irradiation effects in the electronic properties of atomic layers of MoS_2. © *2015 American Vacuum Society*. [http://dx.doi.org/10.1116/1.4906331]

I. INTRODUCTION

Transition metal dichalcogenides such as molybdenum disulfide (MoS_2) have attracted great interest as candidates to fill the need of two dimensional semiconductor materials. By controlling the thickness, the bandgap of MoS_2 thin films can be tuned from 1.2 eV (bulk material, indirect bandgap) to 1.8 eV (monolayer film, direct bandgap).[1] Recently, large scale MoS_2 monolayers have been grown by chemical vapor deposition (CVD) on silicon dioxide (SiO_2) substrate,[2–4] showing the possibility of low cost scalable device fabrication. However, measurements on CVD grown MoS_2 monolayers[2–4] reveal mobility values that are usually orders of magnitude lower than those (exceeding 200 $cm^2\ V^{-1}\ s^{-1}$) reported on exfoliated MoS_2 monolayers.[5] The physical origin of the difference between CVD and exfoliated MoS_2 is not clear at present; however, structural defects[6] such as vacancies, dislocations,[7] grain boundaries,[4] as well as charged interfacial states due to the dielectrics in contact[8] can be responsible for the degradation in mobility. Although this problem has presented a major hurdle to the realization of wafer-scale MoS_2 electronics and photonics, systematic studies of defects' role in individual crystal domains are still lacking.

Furthermore, it is known that the use of high-energy particle irradiation on semiconductor nanostructures can drastically modify their electronic properties. Durand *et al.*[9] have shown that InAs nanowires exhibiting n-type semiconducting behavior turn metallic under electronic irradiation. On MoS_2, long range magnetic ordering in bulk crystal[10] has been demonstrated after irradiation with a 2 MeV proton beam. At higher beam energy (10 MeV), a time dependent transport behavior has been observed in MoS_2 field effect transistors[11] and related to the formation of charge traps in dielectric material and its interface with the MoS_2 (few layers) channel. In the case of electronic irradiation, Komsa *et al.*[12] have reported that an electron beam energy about 90 keV is necessary to create sulfur vacancies in MoS_2 by knock-on mechanism. Such defect engineering presents a lot of attractive possibilities to tune the properties of this material and also to create new kinds of nanostructure, like Mo_5S_4 nanoribbons.[13,14] Recently, Zhou *et al.*[6] suggest that vacancies can form even in the energy range provided by scanning electron microscope (SEM, 30 keV) under electron beam exposure. Although electron beam techniques are widely used in microscopic imaging and nanofabrication processes, the effect of electron beam irradiation on the transport properties of MoS_2 atomic layer has not been evaluated, especially at low beam energy regime.

Here, we study the transport properties of CVD-grown monolayer on SiO_2/Si substrate by directly measuring the resistivity and the mobility of the material with a field-effect transistor configuration with the use of a cryogenic four-probe scanning tunneling microscope (STM).[15,16] The combination of the STM scanners and a SEM enables us to connect the STM tips on individual MoS_2 domains. The temperature dependent resistivity and mobility show a defect dominated transport process. Furthermore, the effects of electronic irradiation are examined by exposing the film to

[a)]Electronic mail: apli@ornl.gov

electron beam in the SEM in an ultrahigh vacuum environment, and it is found that a clear change of transport behavior of the material after electronic irradiation with SEM at low energy (5 keV). It is suggested that the presence of defects create charge trapping states and leads to the low mobility, consistent with recent theoretical calculations[17,18] where vacancies and antisites defects are shown to create localized gap states.

II. EXPERIMENT

The synthesis of monolayer MoS_2 domains by CVD process has been described by Najmaei *et al.*[2] Briefly, MoO_3 nanoribbons and sublimated sulfur are used as precursors. The MoO_3 nanoribbons are dispersed on silicon substrates and placed close to a bare Si/SiO_2 substrate designated for the growth of MoS_2 at the center of a quartz tube (furnace) under a constant N_2 flow of 200 sccm. And 0.8–1.2 g of sublimated sulfur is placed in a container at the opening of the furnace where the maximum temperature approximately reaches 600 °C. At a rate of approximately 20 °C/min, the center of the furnace is gradually heated from room temperature to 550 °C in 30 min. The sulfur slowly evaporates when the temperature reaches approximately 550 °C. Then, at the slower ramping rate of ~5 °C/min, the chamber is heated to 850 °C. This temperature is maintained for 10–15 min and then the system is naturally cooled back to room temperature.

The as-grown sample is studied with a four-probe scanning tunneling microscope (4P-STM), a characterization platform combining four STM and a SEM operating in ultrahigh vacuum (UHV)[15] (base pressure $< 5 \times 10^{-10}$ Torr). The 4P-STM enables the positioning of four STM electrochemically etched tungsten tips in an arbitrary arrangement under SEM view. This tool provides the capability of establishing contacts on surfaces and nanostructures with the resolution offered by the STM scanners.[19]

STM tips can act as electrodes and provide good contacts on metals and some doped semiconductors.[16] Here, our study focuses on single MoS_2 monolayers lying on a 300 nm thick SiO_2 substrate, a subnanometer thick semiconductor with a bandgap of around 1.8 eV on an insulator. Unlike measurements on graphene,[20] it turns out very challenging to establish reliable electrical contacts between the STM tips and the MoS_2 by gentle contacts without damaging the monolayer. In order to ensure reliable electrical contacts, platinum pads have been deposited by using electron beam induced deposition (EBID)[21] at several locations on MoS_2 domains [Fig. 1(a)]. As reported by Das *et al.*,[22] Sc and Ti would be better choices than Pt due to their lower work function values, which can facilitate the carrier injection process to the MoS_2. Here, we choose Pt because of the availability of the sources in our EBID technique. However, as will be shown later, we still obtain an ohmic contact and the contact resistance has been taken into account in our analysis.

The EBID experiments were conducted in an FEI Nova 600 dual ion/electron microscope. A focused beam of electrons (5 keV, 1.6 nA, and diameter ~300 nm) was used to partially dissociate substrate absorbed, organometallic precursor molecules, resulting in a condensed deposit. Notably, secondary electrons, created during inelastic primary electron–substrate interactions, ultimately lead to precursor dissociation at the sample surface during EBID. The precursor molecule was a platinum based, organometallic compound *trimethyl(methylcyclopentadienyl)platinum(IV)* $[C_5H_4CH_3Pt(CH_3)_3]$. The precursor was delivered to the MoS_2 covered surface by an injection nozzle located 100 μm above the sample surface. The nozzle makes it possible to achieve a relatively high local pressure of precursor (~10 mTorr) without compromising the high vacuum requirement in the electron optics column. The injection nozzle was 500 μm diameter. The resulting deposit contained a mixture of Pt nanoparticles embedded in an amorphous carbon matrix. The composition of the deposit following EBID was ~PtC_5 according to qualitative energy dispersive spectroscopy measurements. Deposit composition was not quantified because the sample heating cycle, following EBID and required for sample preparation prior to conducting electrical measurements, was certain to remove additional carbon from the deposit, which is a well-documented phenomenon that occurs when heating EBID deposits.[21,23] Direct write experiments were initiated when the sample chamber was evacuated to a base pressure on the order of ~7.5×10^{-6} Torr. A deposit with typical lateral dimensions of ~4 μm × 4 μm was deposited by multiple raster scans of the electron beam. Care was taken to minimize electron exposure outside the deposition zone by avoiding electron beam imaging following deposition; only after flushing the chamber with N_2, up to atmospheric pressure, was electron imaging conducted for characterization purposes. The deposition zone direct-write pattern was a square array of pixels with a pixel spacing of 73.3 nm. The electron beam dwell time per pixel was 100 μs. Multiple beam passes (200) are used in order to avoid precursor surface depletion in the growth zone that can occur for relatively long beam dwell times or high beam current densities. This looping tactic effectively minimizes the dose of electrons, thereby minimizing MoS_2 electron exposure. A final deposit height of ~250 nm resulted.

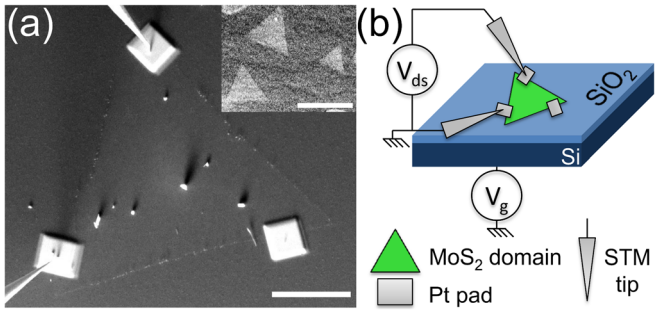

FIG. 1. (Color online) (a) SEM image of single MoS_2 grain grown on a SiO_2 substrate with three Pt pads deposited. Two STM tips are connected on the upper and left pads. Scale bar 10 μm. Inset: SEM image of single grains without Pt pad. Scale bar: 20 μm. (b) Schematics view of the measurement setup.

The sample is annealed at 135 °C for 8 h in the load–lock of the UHV system (base pressure lower than 5×10^{-8} Torr) before being transferred onto the STM platform. Recent studies[24,25] suggested a higher annealing temperature (above 250 °C) of MoS_2. Here, we anneal the sample at lower temperature for a longer time in order to minimize the effect of metal diffusion, a process not being well examined on monolayer CVD MoS_2. The SEM image in the inset of Fig. 1(a) shows MoS_2 monolayer islands grown on a SiO_2 layer. Those domains have a triangular shape with a size ranging from a few micrometers to few tens of micrometers. The main SEM image shows a single domain on which Pt pads have been deposited at each corner of the triangle (bright squares). The STM probes are directly connected onto the Pt pads.

III. RESULTS AND DISCUSSION

The transport measurements are realized with the configuration depicted in Fig. 1(b). The source–drain current I_{ds} versus the voltage V_{ds} is measured by the two probes in contact with the MoS_2 domain whereas the back gate voltage V_g is applied to the heavily doped p-type Si substrate, with the thermally grown SiO_2 serving as gate dielectric material.

At room temperature, the $I_{ds}(V_{ds})$ curves is linear (Fig. 2) up to 20 V (not shown here) even with a gate voltage V_g ranging from −200 to +200 V, indicating that the Pt pads provide Ohmic contacts to the MoS_2. The $I_{ds}(V_g)$ curve (Fig. 2) has typical characteristics for a n-type field effect transistor, as previously observed for MoS_2 films grown with this method.[2] In the linear region of the transfer characteristic $I_{ds}(V_g)$, the source–drain current I_{ds} is given by[26,27]

$$I_{ds} \cong \frac{W}{L} \times C \times \mu_{FE} \times \left[(V_g - V_T) V_{ds} - \frac{V_{ds}^2}{2} \right], \quad (1)$$

where V_T is a threshold voltage that can be deduced from the linear extrapolation of the $I_{ds}(V_g)$ characteristic, and we assume that the mobility is only slowly varying with V_g in the linear region of the $I_{ds}(V_g)$ characteristics. The square term of V_{ds} can be neglected under the condition $V_g \gg V_{ds}$. The field effect mobility (μ_{FE}) is extracted from the transconductance $g_m = dI_{ds}/dV_g$ using[5,26–28]

$$\mu_{FE} = \frac{L}{CW} \times \frac{1}{V_{ds}} \times g_m, \quad (2)$$

where L and W are the length and the width of the channel, respectively, and C is the normalized gate capacitance per unit area. The measured mobility is 0.029 $cm^2\ V^{-1}\ s^{-1}$, a low value compared to previous reports on large MoS_2 films.[2,3] The temperature dependent transport behaviors are measured from 140 to 315 K. Figure 3(a) shows the evolution of the mobility as a function of the temperature at $V_g = 200$ V. The measured μ_{FE} (solid squares) increases with the temperature, as expected for a semiconductor.

The mobility can also be calculated from the channel conductance using[26]

$$g_d = \frac{dI_{ds}}{dV_{ds}} = \frac{W}{L} \times \mu_{FE} \times C \times (V_g - V_T). \quad (3)$$

However, the two terminal configurations we use implies that our measurements are affected by the contact resistances R_C as compared to mobility measurements with a multiterminal configuration.[29,30] Following Horowitz *et al.*,[27] we introduce the contact resistances R_C in the expression of the source–drain current I_{ds} (the square term of V_{ds} being neglected) by changing V_{ds} to $V_{ds} - I_{ds} \times R_C$. Then, the expression for the channel conductance Eq. (3) becomes

$$g_d = \frac{(W/L)\, C \mu_{eff} (V_g - V_T)}{1 + (W/L)\, C \mu_{eff} R_C (V_g - V_T)}, \quad (4)$$

μ_{eff} being the "effective mobility." As suggested by Horowitz *et al.*,[27] the mobility can be assumed to follow an empirical law of the form

$$\mu_{eff} = \alpha (V_g - V_T)^{\beta}. \quad (5)$$

Performing a least squares fit of the data gives us an estimation of the contact resistances R_C. The contact resistances (not shown) is found to decrease with the increasing temperature and account for 10% to 40% of the total resistance in our temperature range and V_g from 100 to 200 V. Once we have estimated the contact resistances, we recalculate the effective mobility μ_{eff} from the channel conductance using Eq. (4). The values at $V_g = 200$ V are shown in Fig. 3(a), represented by the empty squares. One can see that μ_{eff} is higher by a factor 2–3 than μ_{FE}, which means that the contact resistances do play a role in our system. Moreover, the mobility changes slightly with the applied gate bias after considering the contact resistance even for $V_g \gg V_{ds}$ as shown in Fig. 3(b).

Above analysis indicates that the mobility in MoS_2 has a strong temperature dependence as well as a weak gate voltage dependence. This is consistent with a multiple trapping and release (MTR) model described by Horowitz *et al.*[27] The MTR model requires that most of the charge carriers are

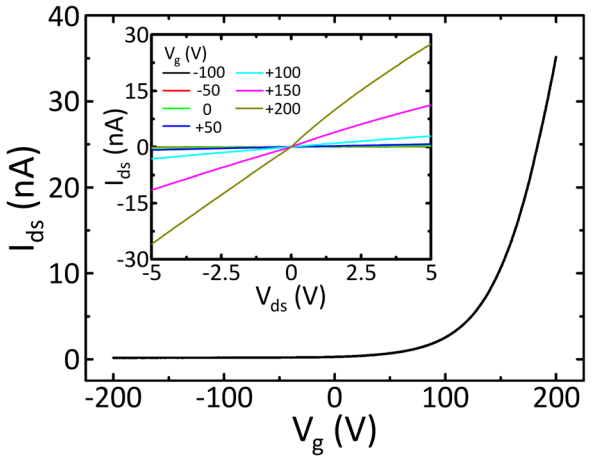

FIG. 2. (Color online) Room-temperature $I_{ds}(V_g)$ transfer characteristic for a single MoS_2 domain with the field-effect transistor configuration described in the main text with 5 V applied bias voltage V_{ds}. Inset: $I_{ds}(V_{ds})$ characteristics at different gate voltage V_g.

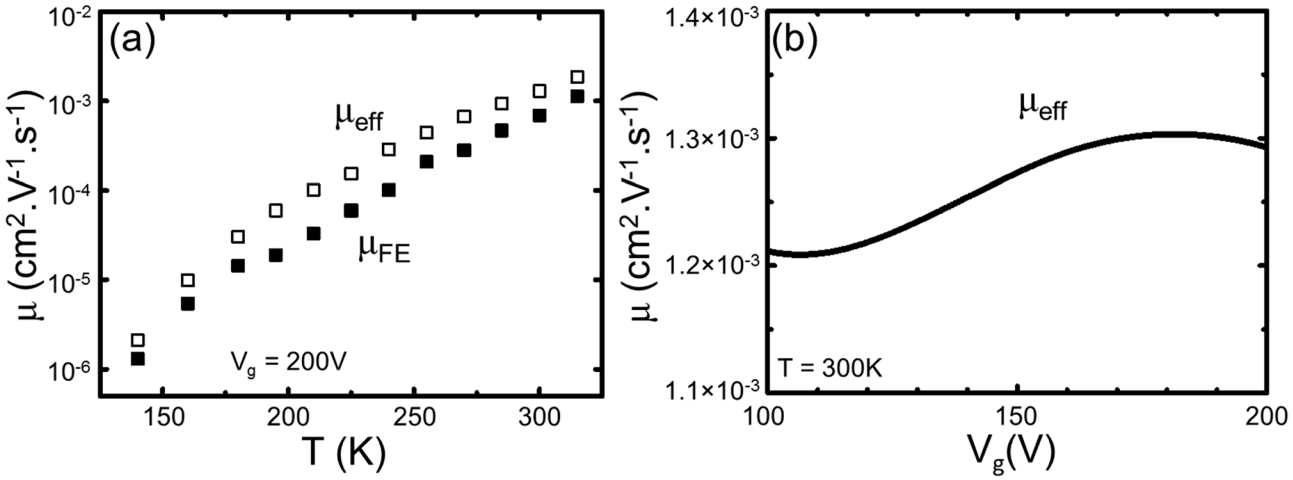

FIG. 3. (a) Field-effect μ_{FE} mobility (solid squares) as a function of temperature extracted at $V_g = 200$ V from the transconductance g_m as a function of the temperature [Eq. (2)]. The empty squares represent the effective mobility μ_{eff} (same V_g) calculated with the channel conductance Eqs. (4) and (5). (b) The effective mobility as a function of gate bias voltage at 300 K after considering the contact resistances [Eqs. (4) and (5)].

trapped in localized states. The amount of released charge carriers to an extended-state that contributes to transport depends on the energy level of the localized states, the temperature, and the gate voltage, leading to a thermally activated mobility. In such a trap-limited transport model, transport occurs only in delocalized bands. This is in sharp contrast to the mechanism of variable range hopping, which is often invoked as the transport mechanism in MoS_2, where all trap levels participate in hopping conduction and contribution from delocalized carriers is absent.

Figure 4 shows the effective mobility μ_{eff} at several different V_g as a function of the inverse of the temperature, R_C being subtracted. Indeed, μ_{eff} can be modeled with thermally activated transport:

$$\mu_{eff} \sim \exp\left[-\frac{E_a}{k_B T}\right], \tag{6}$$

where E_a is the activation energy and k_B the Boltzmann constant. With V_g increasing, the activation energy E_a decreases slightly (from 150 for 144 meV when V_g increases from 140 to 200 V), in agreement with the MTR model and previously reported behaviors of MoS_2.[17,29,30] Note, we have tried to fit the temperature dependence of μ and of the resistivity ρ with the variable-range hopping equation for 2D materials

$$\mu_{eff} \sim \exp\left[-\left(\frac{T_0}{T}\right)^{\frac{1}{3}}\right] \tag{7}$$

and

$$\rho \sim \exp\left[\left(\frac{T_0}{T}\right)^{\frac{1}{3}}\right] \tag{8}$$

and obtained a fitting parameter $T_0 = 2.8 \times 10^6$ K that is orders of magnitude higher than observed for exfoliated MoS_2.[8,17,31]

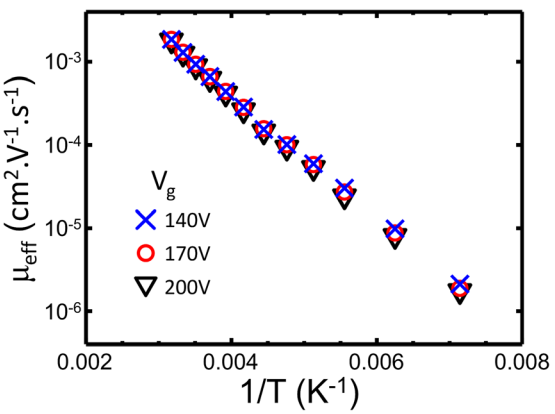

FIG. 4. (Color online) Effective mobility as a function of the inverse of the temperature at different gate voltage. Arrhenius plots give activation energy in the range of 144–150 meV.

The mobility values presented above are very low compared to the intrinsic limit reported for MoS_2 monolayers (410 cm^2 V^{-1} s^{-1}).[32] TEM studies on CVD grown MoS_2 islands similar to what we used in this work[2] showed the good quality of the monolayer islands, and also revealed the presence of different structural defects like sulfur vacancies.[6] In addition to the trap states at the interface between the dielectric and the channel,[8] these structural defect can lead to localized electronic states.[6,17] In their recent studies, Zhu *et al.*[30] demonstrated that the presence of a large amount of localized traps leads to the smearing of the band edge and the formation of band tail states in the MoS_2 energy gap. The mobility edge forms a boundary in the band tail, which separates extended states with band transport and localized states that conduct via thermally assisted mechanisms. Based on the subthreshold swing (SS) extracted from $I_{ds}(V_g)$ curves, we can estimate the value of trap density D_{it} with the formula[26]

$$SS \cong \ln 10 \times \frac{kT}{q}\left(1 + \frac{C_D + C_{it}}{C}\right) = \ln 10 \times \frac{kT}{q}\left(1 + \frac{C_D + qD_{it}}{C}\right), \tag{9}$$

where C_D and C_{it} are the capacitance associated to the depletion-layer and the traps, respectively, and q the elementary charge. For this device, SS is very large, in the range of 225–275 V/dec, compared to other reports on CVD MoS_2 monolayers (200 mV/dec for Ref. 30, 13 V/dec in Ref. 3). In that case, we assume $C_{it} \gg C_D$ and find a density of trap state in the $10^{14}\,eV^{-1}\,cm^{-2}$ range. Such a high value of D_{it} corroborates the MTR model.

To further examine the role of defects in the transport of MoS_2, we now study the impact of the electronic irradiation. Figure 5(a) shows the conductance measured at room temperature and $V_g = 100$ V as a function of time with several irradiation events with a 5 kV electron beam. Since the connection of the STM tips onto the Pt requires real time SEM imaging, the first measurement (black star and black curve in the inset) has been performed around 30 min after electron beam irradiation (first irradiation). During transport measurements, the electron beam is turned off. After one additional SEM imaging scan (~2 min for the whole frame, second irradiation event indicated in red arrow), the conductance is multiplied by a factor 2, as shown by the first red square in Fig. 5(a) and upper red $I_{ds}(V_{ds})$ curves in the inset. The conductance becomes time dependent with a slow relaxation process. Another factor 2 of increase of conductance is observed after the third irradiation event [Fig. 5(a), upper arrow], which then starts to relax and reaches its original value after 6×10^4 s [Fig. 5(a), blue squares]. Figure 5(b) shows the time dependence of the current on another MoS_2 domain at $V_{ds} = 5$ V, $V_g = 0$ V and room temperature. The measurement starts several seconds after an irradiation event and shows that the current decreases by about 20% after 15×10^3 s. The mobility [Fig. 5(b), inset] drops noticeably after the second irradiation event (marked by the black arrow) and then gradually recovers its initial value. Thus, the rise in the conductivity after irradiation [Fig. 5(a)] is due to an increase of the carrier concentration. Unlike the InAs nanowires which turn metallic,[9] monolayer MoS_2 keeps semiconducting. Moreover, the irradiation effect has not been observed at $T \leq 140$ K for MoS_2, and the current recovers its original value instantaneously without decaying process.

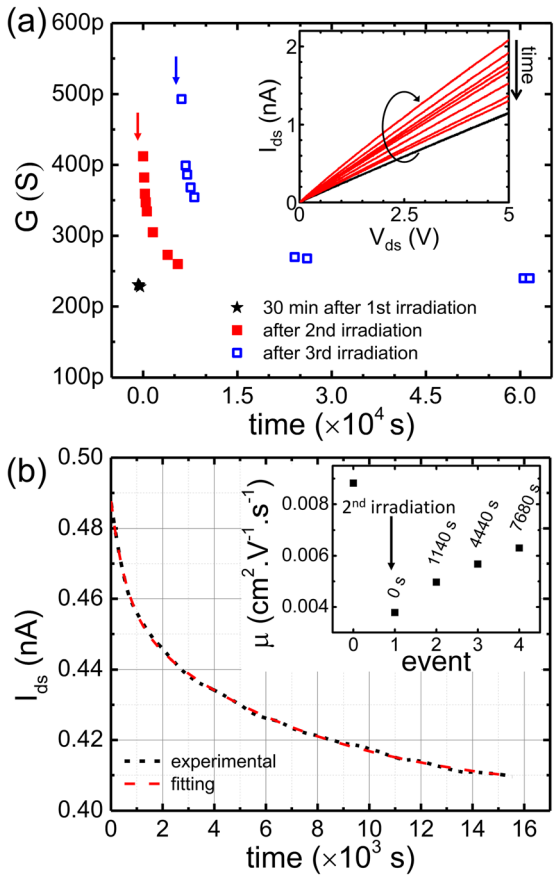

FIG. 5. (Color online) (a) Time dependence of the conductance measured at $V_g = +100$ V after three irradiation events. Inset: $I_{ds}(V_{ds})$ curves after first and second irradiation events, corresponding to the black star and the solid squares of the main graph, respectively. (b) I_{ds} vs time measured at $V_{ds} = 5$ V and $V_g = 0$ V after irradiation [MoS_2 domain different from (a)]. The dashed curve is fitted with $y = y_0 + A_1 e^{-(x-x_0)/t_1} + A_2 e^{-(x-x_0)/t_2}$, where the times constants $t_1 = 600$ s and $t_2 = 7100$ s. Inset: Mobility values of the same domain before and after second irradiation event (arrow) measured at different time as indicated.

The subthreshold swing of the device that is irradiated with an electron beam becomes worse, as shown in Fig. 6(a). Such degradation of the subthreshold swing after irradiation is similar to that observed on MoS_2 irradiated by proton beams[11] and can be attributed to the irradiation-induced trap states at the interface of MoS_2 and SiO_2. Based on the subthreshold swing extracted from $I_{ds}(V_g)$ curves, we can estimate the value of trap density D_{it} after the irradiation event as plotted in Fig. 6(b) (solid squares), which are even higher than observed before irradiation. Moreover, as shown in Fig. 6(b) (empty squares, right axis), the threshold voltage V_{th} shifts toward negative value after irradiation (event 1 in red), indicating an increase of the carrier concentration, in agreement with the observation on conductance change.

The interface trap states induced by irradiation process affect the Fermi level position of the conduction channel and thus the carrier concentration, which is consistent with our observed shift of the threshold voltage and those reported by Kim *et al.*[11] Moreover, we find that the interface trap states and the carrier density vary over a different time scale. Figure 6(b) shows that the interface trap density increase from $1.42 \times 10^{14}\,cm^{-2}\,eV^{-1}$ (event 0, not shown on the graph) to $1.67 \times 10^{14}\,cm^{-2}\,eV^{-1}$ after irradiation (event 1, red filled square) and then, following exponential decay with a time constant ~600 s. On the other side, the carrier concentration, related to the threshold voltage shift ΔV_{th} [Fig. 6(b), empty squares], varies with a much higher the time constant of ~2600 s. Thus, the interface trap states density alone cannot account for the change of carrier concentration in the conduction channel. Interestingly, the conductance change after irradiation also shows a two component decay behavior [as shown with the fitting curve in Fig. 5(b)] and one component has almost the same time constant as the interface trap density. All these observations show that both the defects created in active MoS_2 layer and trap states at the interface of MoS_2/SiO_2 are responsible for the peculiar conductance relaxation process. We would like to mention that we have studied the influence of the electron beam energy on the I(V) characteristics of MoS_2 by varying the

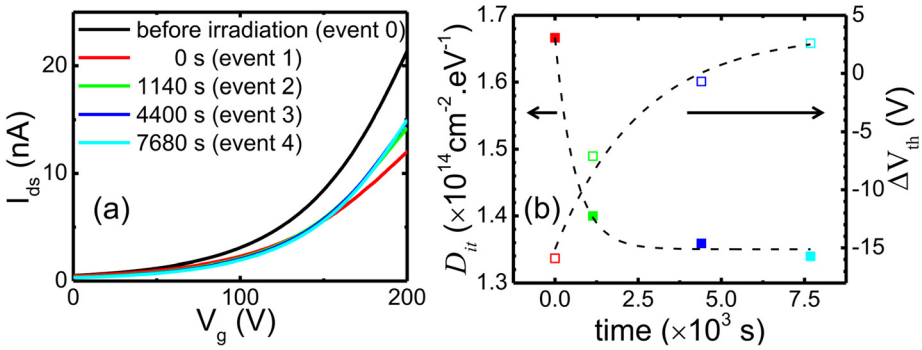

FIG. 6. (Color online) (a) $I_{ds}(V_g)$ characteristics before (upmost curve) and after (lower curves) an irradiation event (same dataset as the inset of Fig. 4(b) with event number reported). The lowest curve (event 1) is measured right after the irradiation event (0 s). (b) Trap density D_{it} (filled squares, left axis) deduced from the subthreshold swing and shift of the threshold voltage ΔV_{th} (empty squares, right axis) after irradiation extracted from (a) with corresponding colors (event 0 not shown). The dashed lines are fitting curves with $y = y_1 + A_3 e^{-(x-x_1)/t_3}$ and time constant $t_3 = 600$ and 2600 s for D_{it} and ΔV_{th}, respectively.

acceleration voltage of the SEM in the range of 0.5–11 kV and have not observed any significant change of the transport behavior in this range.

As mentioned previously, it has been demonstrated that electron irradiation creates sulfur vacancies in MoS_2.[12] While the electron beam energy used in our experiment (5 keV) may be too low to create defects by electron-beam sputtering process,[33] beam damage through inelastic scattering process still occurs even at low energy through, e.g., a radiolysis effect[33] and can create defects in MoS_2 under SEM.[6] Moreover, as reported by Egerton *et al.*,[33] radiolysis is temperature dependent and can be reduced by cooling the sample, and this is consistent with fact that our sample is less subjected to the electronic irradiation damage at low temperature $T = 140$ K although a charging effect is still noticeable at low temperatures.

It is noted that a transition from a bandlike electronic transport to transport via thermally activated mechanism, a metal to insulator transition, has been observed in MoS_2 by tuning the carrier density or suppressing the interface charge effect. For example, Radisavljevic and Kis have demonstrated the use of the high-k dielectric HfO_2 as a top gate significantly improved the screening of the Coulomb interactions induced by the backgate MoS_2/SiO_2 interface.[29] Consequently, a metallic transport with much improved mobility has been achieved.[29] Similarly, in our case, high density of charge trap states can be created by the electron irradiation at the MoS_2/SiO_2 interface. The charge trap states may strongly screen the electric field of the backgate, leading to a constant insulating regime over the wide range of gate voltage and preventing a transition to the metallic regime. This observation highlights the important effect of electron beam, commonly used in imaging and fabrication techniques, on the device performance.

IV. SUMMARY

We have studied temperature-dependent electrical transport in individual domains of monolayer MoS_2 grown by CVD onto Si/SiO_2 substrates. We find that the electrons are mostly localized well up to room temperature and display multiple charge trapping and release behavior. We show electron irradiations can significantly affect the transport by increasing the carrier density and reducing the mobility. These effects are likely to arise from scattering by the intrinsic defects in MoS_2 and the Coulomb potential of randomly distributed charges at the MoS_2/SiO_2 interface induced by electronic irradiation. Highly improved device performance should consider reducing defects in the active MoS_2 layer, avoid electron beam irradiations, or suppressing the screening effect of the interface charges by appropriate device engineering.

ACKNOWLEDGMENTS

This research was conducted at the Center for Nanophase Materials Sciences, which is sponsored at Oak Ridge National Laboratory by the Scientific User Facilities Division, Office of Basic Energy Sciences, U.S. Department of Energy. A portion of theory work (C.D.) was supported by the Laboratory Directed Research and Development Program of Oak Ridge National Laboratory, managed by UT-Battelle, LLC, for the U. S. Department of Energy.

[1]A. Splendiani, L. Sun, Y. Zhang, T. Li, J. Kim, C.-Y. Chim, G. Galli, and F. Wang, Nano Lett. **10**, 1271 (2010).
[2]S. Najmaei *et al.*, Nat. Mater. **12**, 754 (2013).
[3]H. Liu, M. Si, S. Najmaei, A. T. Neal, Y. Du, P. M. Ajayan, J. Lou, and P. D. Ye, Nano Lett. **13**, 2640 (2013).
[4]A. M. van der Zande *et al.*, Nat. Mater. **12**, 554 (2013).
[5]B. Radisavljevic, A. Radenovic, J. Brivio, V. Giacometti, and A. Kis, Nat. Nanotechnol. **6**, 147 (2011).
[6]W. Zhou *et al.*, Nano Lett. **13**, 2615 (2013).
[7]X. Zou, Y. Liu, and B. I. Yakobson, Nano Lett. **13**, 253 (2013).
[8]S. Ghatak, A. N. Pal, and A. Ghosh, ACS Nano **5**, 7707 (2011).
[9]C. Durand, M. Berthe, Y. Makoudi, J.-P. Nys, R. Leturcq, P. Caroff, and B. Grandidier, Nanotechnology **24**, 275706 (2013).
[10]S. Mathew *et al.*, Appl. Phys. Lett. **101**, 102103 (2012).
[11]T.-Y. Kim, K. Cho, W. Park, J. Park, Y. Song, S. Hong, W.-K. Hong, and T. Lee, ACS Nano **8**, 2774 (2014).
[12]H.-P. Komsa, J. Kotakoski, S. Kurasch, O. Lehtinen, U. Kaiser, and A. V. Krasheninnikov, Phys. Rev. Lett. **109**, 035503 (2012).
[13]X. Liu *et al.*, Nat. Commun. **4**, 1776 (2013).
[14]H.-P. Komsa, S. Kurasch, O. Lehtinen, U. Kaiser, and A. V. Krasheninnikov, Phys. Rev. B **88**, 035301 (2013).
[15]T.-H. Kim, Z. Wang, J. F. Wendelken, H. H. Weitering, W. Li, and A.-P. Li, Rev. Sci. Instrum. **78**, 123701 (2007).
[16]A.-P. Li, K. W. Clark, X. G. Zhang, and A. P. Baddorf, Adv. Funct. Mater. **23**, 2509 (2013).
[17]H. Qiu *et al.*, Nat. Commun. **4**, 2642 (2013).

[18]J. D. Fuhr, A. Saúl, and J. O. Sofo, Phys. Rev. Lett. **92**, 026802 (2004).
[19]S. Qin, T.-H. Kim, Z. Wang, and A.-P. Li, Rev. Sci. Instrum. **83**, 063704 (2012).
[20]K. W. Clark, X. G. Zhang, I. V. Vlassiouk, G. He, R. M. Feenstra, and A.-P. Li, ACS Nano **7**, 7956 (2013).
[21]A. Botman, J. J. L. Mulders, and C. W. Hagen, Nanotechnology **20**, 372001 (2009).
[22]S. Das, H.-Y. Chen, A. V. Penumatcha, and J. Appenzeller, Nano Lett. **13**, 100 (2013).
[23]N. A. Roberts, J. D. Fowlkes, G. A. Magel, and P. D. Rack, Nanoscale **5**, 408 (2013).
[24]S. Tongay *et al*., Nano Lett. **13**, 2831 (2013).
[25]R. Yang, X. Zheng, Z. Wang, C. J. Miller, and P. X.-L. Feng, J. Vac. Sci. Technol., B **32**, 061203 (2014).
[26]S. M. Sze, *Physics of Semiconductor Devices* (Wiley, New York, 1981).
[27]G. Horowitz, M. E. Hajlaoui, and R. Hajlaoui, J. Appl. Phys. **87**, 4456 (2000).
[28]A. R. Völkel, R. A. Street, and D. Knipp, Phys. Rev. B **66**, 195336 (2002).
[29]B. Radisavljevic and A. Kis, Nat. Mater. **12**, 815 (2013).
[30]W. Zhu, T. Low, Y.-H. Lee, H. Wang, D. B. Farmer, J. Kong, F. Xia, and P. Avouris, Nat. Commun. **5**, 3087 (2014).
[31]D. Jariwala, V. K. Sangwan, D. J. Late, J. E. Johns, V. P. Dravid, T. J. Marks, L. J. Lauhon, and M. C. Hersam, Appl. Phys. Lett. **102**, 173107 (2013).
[32]K. Kaasbjerg, K. S. Thygesen, and K. W. Jacobsen, Phys. Rev. B **85**, 115317 (2012).
[33]R. F. Egerton, P. Li, and M. Malac, Micron **35**, 399 (2004).